

Active Damping of Boring Bar Vibration With a Magnetic Actuator

Fan Chen, Masih Hanifzadegan, *Student Member, IEEE*, Yusuf Altintas, and Xiaodong Lu, *Member, IEEE*

Abstract—Boring bars with a large length-to-diameter ratio chatter under productive cutting conditions, which leads to poor surface finish and violation of part tolerances. This paper presents an active damping method of boring bars with an in-house designed magnetic actuator. The actuator has been designed to have a linear force output relative to the input current, and instrumented to control boring bar vibrations. Four different H_∞ optimal controllers are designed to shape the boring bar dynamics and improve the chatter stability. The proposed active damping method is experimentally tested on a CNC lathe. The dynamic stiffness of the boring bar is increased considerably, leading to a significant increase in the chatter-free material removal rates.

Index Terms—Active damping, boring bar, magnetic actuator, chatter.

I. INTRODUCTION

BORING is a commonly used operation for enlarging holes. When boring large and long diesel engine cylinder walls or similar parts, very long and flexible boring bars have to be used. However, for boring bars with a large length-to-diameter ratio, the productivity is constrained due to their excessive flexibility. The long boring bars statically deflect under cutting loads and chatter when the depth of cut exceeds stability limits, which leads to tolerance violations and poor surface finish. For a fine boring process, the surface roughness (R_a) is usually required to be less than 1 μm . However, once chatter happens, the surface roughness can easily reach more than 6 μm . In rough machining, however, the unstable cutting, i.e., chatter, the vibration amplitudes of slender boring bars can reach to 500 μm , and the magnitude of the applied force would triple which will damage the costly parts and machine tools. The static stiffness of the boring bar needs to be increased to reduce static deflections, and the dynamic stiffness must be improved to minimize the chatter vibrations. The dynamic stiffness of the boring bars can be increased either by passive or active damping methods.

Manuscript received July 4, 2014; revised September 17, 2014 and November 17, 2014; accepted January 14, 2015. Date of publication February 24, 2015; date of current version October 21, 2015. This work was supported by the NSERC CANRIMT grant (Canada PG 11R47093) and the China Scholarship Council.

F. Chen is with the Manufacturing Automation Laboratory and Precision Mechatronics Laboratory, Department of Mechanical Engineering, The University of British Columbia, Vancouver, BC V6T 1Z4, Canada (e-mail: fan.chen@alumni.ubc.ca).

M. Hanifzadegan is with the Control Engineering Laboratory, Department of Mechanical Engineering, The University of British Columbia, Vancouver, BC V6T 1Z4, Canada (e-mail: masih.hanif@alumni.ubc.ca).

Y. Altintas is with the Manufacturing Automation Laboratory, Department of Mechanical Engineering, The University of British Columbia, Vancouver, BC V6T 1Z4, Canada (e-mail: altintas@mech.ubc.ca).

X. Lu is with the Precision Mechatronics Laboratory, Department of Mechanical Engineering, The University of British Columbia, Vancouver, BC V6T 1Z4, Canada (e-mail: xdlu@mech.ubc.ca).

Color versions of one or more of the figures in this paper are available online at <http://ieeexplore.ieee.org>.

Digital Object Identifier 10.1109/TMECH.2015.2393364

A variety of passive vibration absorbers have been proposed in the literature for boring bars [1]. The passive damping methods require the attachment of a mass–spring–damper system to the boring bar with an identical frequency which needs to be damped. Godfrey used a carbide tool shank with a built-in passive damper to improve the performance of boring bars [2]. Miguelez *et al.* [3] considered the parameters of passive dynamic absorbers into the chatter stability model, and the absorber parameters were determined by optimizing the chatter stability. Yang *et al.* [4] presented an optimal tuning method for multiple tuned mass dampers to increase chatter stability. The parameters of the dampers are tuned to maximize the minimum negative real part of the frequency response function (FRF) at the tool–workpiece interface. However, it is difficult to damp several modes with tuned dampers when the space is limited as in the case of boring bars. Furthermore, the natural frequency of the system may differ in each application, and tuned, passive dampers need to be remanufactured for each mode.

The active methods allow damping of several modes simultaneously by adjusting the control parameters of the actuators. Tanaka *et al.* [5] installed eight piezo actuators into a boring bar for active damping. An accelerometer was used to measure the boring bar vibration at the tool tip, and a velocity feedback controller is implemented to actively damp the vibrations. Redmond *et al.* [6] installed four piezo actuators inside a boring bar with acceleration feedback control for active damping. Pratt and Nayfeh [7] installed two Terfenol-D actuators outside the boring bar and used a dynamic compensator in the control system to make the actuators behave like an active vibration absorber. A survey of the active damping of spindle vibrations is presented by Abele *et al.* [8]. A set of piezo actuators has been installed behind the outer rings of the spindle bearings for active damping with various control strategies [8]. However, both piezo and Terfenol-D actuators have hysteresis [9]–[17], which needs to be modeled and compensated during the controller design process, therefore complicating the design of linear controllers. Noncontact magnetic actuators can have a large load capacity and almost no hysteresis, and they have been implemented in the active control of chatter during machining. Chen and Knospe [18] installed a magnetic bearing into a lathe, and designed three different controllers based on μ synthesis to optimize chatter stability. Van Dijk *et al.* [19] implemented a magnetic bearing in the milling spindle. The spindle speed and depth of cut were treated as uncertainties, and μ synthesis is used to design a robust controller to guarantee the cutting stability for the predefined range of spindle speed and depth of cut. The regenerative time delay in the dynamics of the cutting process was considered in the plant model for controller design, which led to a very high order controller which is difficult to implement in real time [18], [19]. The piezo and Terfenol-D actuators have hysteresis, and magnetic actuators proposed in the past have a nonlinear

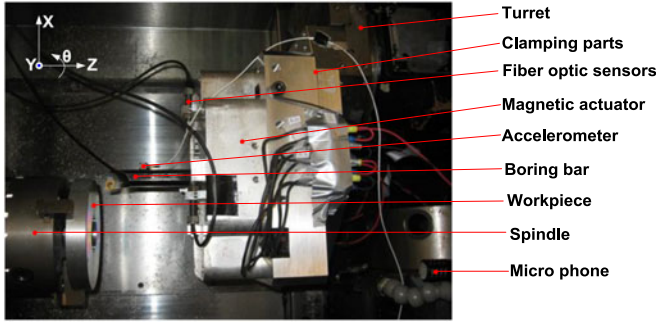


Fig. 1. Experimental setup for active damping of boring bar.

relationship between the delivered force and the commanded current, and hence, their output must be linearized before they can effectively be used in active damping.

A different strategy for the active damping of boring bars is proposed in this paper. A magnetic actuator with a linear relationship between the controlled current and output force has been designed, and is proven to damp a single mode with a simple derivative controller as presented in [20]. The details of the magnetic actuator design principle were given in [25]. In this paper, multiple modes of a boring bar are damped using H_∞ optimal controllers with the developed magnetic actuator, leading to a significant increase in the dynamic stiffness and chatter-free material removal rates.

II. EXPERIMENTAL SETUP AND MODEL IDENTIFICATION

A. Experimental Setup

The active damping algorithm has been tested on the magnetic actuator built and installed on a turning center as shown in Fig. 1. The detail of the actuator was given in [25], but is briefly summarized here for clarity. The force generated by four identical magnetic units of the actuator is linearized with respect to the input current by the design strategy given in [21]. The actuator has three degrees of freedom in two radial (x, y) and angular (θ) directions to damp bending and torsional vibrations which are monitored by using fiber optic sensors at the armature location. The armature of the actuator is clamped to a 305-mm-long Valenite A16T-SCLPR4 boring bar (1 in diameter) using a trans-torque bushing. The boring bar is cantilevered to the clamping part, which carries the stators of the actuator. An accelerometer is attached to the boring bar slightly away from the tool tip to avoid interference with the cutting process.

The system has been tested in boring an aluminum 6061 T6 cylinder with 150 mm outer and 40 mm inner diameters. The distance between the boring bar tip and the actuator is 145 mm. An accelerometer and a microphone are used to measure the boring bar vibration and the sound signals, respectively. Four Varedan LA-415s linear power amplifiers, each with 8 kHz current loop bandwidth, are used to drive the magnetic actuator. A dSPACE 1103 controller board is used for controller implementation. Further details of the actuator design can be found in [25].

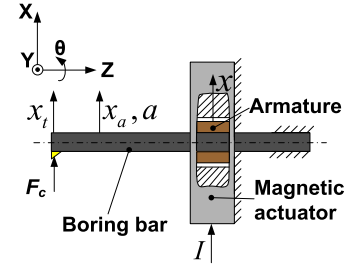


Fig. 2. Diagram of the active damping setup.

B. Model Identification

Based on the modal tests, the boring bar is considered to have uncoupled dynamics in the two radial (x, y) and torsional (θ) directions. The horizontal (y) and torsional (θ) deflections have negligible influence on the regenerative chip thickness, but the dynamic chip thickness is directly affected by the axial (z) and radial (x) deflections in boring [22]. Since the axial stiffness of the boring bar is high, the chatter is caused by the bending modes in the x direction which need to be actively damped by the controller.

The diagram of the boring bar and actuator setup, i.e., plant, is given in Fig. 2. The control current (I) is applied to the magnetic actuator via amplifiers, which leads to magnetic force at the armature that tries to manipulate the boring bar vibrations. The cutting force F_c acts as a disturbance input. The outputs of the plant are the tool tip displacement (x_t), armature displacement (x), boring bar displacement (x_a) and acceleration (a) at the accelerometer location.

The open-loop transfer functions from the input current (I) to displacements (x_t), (x), and (x_a) are denoted by $G_{x_t I}$, $G_{x I}$, and $G_{x_a I}$, respectively. The FRFs are measured by giving an impulse current signal to the current amplifiers and measuring the displacements (x_t) and (x) with fiber optic sensors while measuring the acceleration (a) with the accelerometer. The open-loop transfer functions between displacements (x_t , x_a , x) and the cutting force F_c are denoted by $G_{x_t F}$, $G_{x_a F}$, and $G_{x F}$, respectively. The FRFs are measured with impact hammer tests.

The measured and curve-fitted FRFs of the system are given in Fig. 3, while the estimated modal parameters are given in Table I. It can be seen that the actuator is able to excite mainly the first two modes of the boring bar from its armature location which is 145 mm away from the tool tip. The third mode can hardly be excited by the actuator which makes active damping of the third mode challenging.

The FRFs between the cutting force and boring bar displacements show that the first bending mode of the boring bar at 174 Hz is the most flexible mode, while the third bending mode at 1130 Hz is also quite flexible. However, the second bending mode of the boring bar at 614 Hz can hardly be seen from the measured FRFs of $G_{x_t F}$ [see Fig. 3(f)] and $G_{x I}$ [see Fig. 3(c)]. In order to explore the reason for this, the mode shapes of all the three modes are measured with impact hammer tests (see Fig. 4). An accelerometer is placed at the tool tip to measure the boring bar vibrations, while hammer blows are given at different locations on the boring bar. The measured mode shapes are given in Fig. 4. It can be seen that the fiber optic sensor is

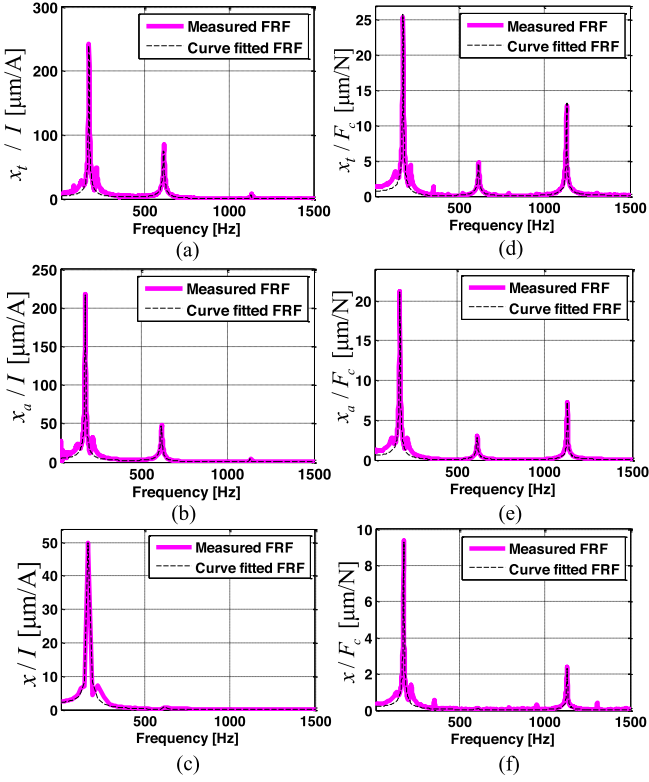


Fig. 3. Measured and curve-fitted FRFs of the plant system. (a) $G_{x_t I}$, (b) $G_{x_a I}$, (c) $G_{x I}$, (d) $G_{x_t F}$, (e) $G_{x_a F}$, and (f) $G_{x F}$.

located at a neutral node of the second bending mode of the boring bar assembly. Therefore, the boring bar vibration at the second modal frequency is too small to be detected by the embedded fiber optic sensor.

The transfer function relations between the inputs F_c , I and outputs x_t , x_a , and x are determined from their estimated modal parameters as follows:

$$\begin{aligned} x_t(s) &= G_{x_t I}(s)I(s) + G_{x_t F}(s)F_c(s) \\ x_a(s) &= G_{x_a I}(s)I(s) + G_{x_a F}(s)F_c(s) \\ x(s) &= G_{x I}(s)I(s) + G_{x F}(s)F_c(s) \end{aligned} \quad (1)$$

with the transfer functions

$$\begin{aligned} G_{p_i}(s) &= \frac{\omega_{ni}^2}{s^2 + 2\zeta_i\omega_{ni}s + \omega_{ni}^2} \\ G_{x_t I}(s) &= \frac{x_t(s)}{I(s)} = \sum_{i=1}^3 \frac{G_{p_i}(s)}{k_{x_t I_i}}; \\ G_{x_t F}(s) &= \frac{x_t(s)}{F_c(s)} = \sum_{i=1}^3 \frac{G_{p_i}(s)}{k_{x_t F_i}} \\ G_{x_a I}(s) &= \frac{x_a(s)}{I(s)} = \sum_{i=1}^3 \frac{G_{p_i}(s)}{k_{x_a I_i}}; \\ G_{x_a F}(s) &= \frac{x_a(s)}{F_c(s)} = \sum_{i=1}^3 \frac{G_{p_i}(s)}{k_{x_a F_i}} \end{aligned}$$

$$\begin{aligned} G_{x I}(s) &= \frac{x(s)}{I(s)} = \sum_{i=1,3} \frac{G_{p_i}(s)}{k_{x I_i}}; \\ G_{x F}(s) &= \frac{x(s)}{F_c(s)} = \sum_{i=1,3} \frac{G_{p_i}(s)}{k_{x F_i}} \end{aligned} \quad (2)$$

where $\omega_{ni} = 2\pi f_{ni}$ and ζ_i are the modal frequency (rad/s) and damping ratio, while $k_{x_t I_i}$, $k_{x_t F_i}$, $k_{x_a I_i}$, $k_{x_a F_i}$, $k_{x I_i}$, and $k_{x F_i}$ are the modal stiffnesses of the mode i . Note that the second bending mode cannot be detected with the embedded fiber optic sensor because the sensor is at its neutral point. As a result, the second mode is neglected in $G_{x I}$ and $G_{x F}$.

III. H_∞ CONTROLLER DESIGN FOR ACTIVE DAMPING OF BORING BAR

The ultimate goal for the active damping of the boring bar is to damp the forced and chatter vibrations at the tool tip (x_t), and increase the maximum chatter-free depth of cut with the designed magnetic actuator. Since the critical depth of cut for chatter stability is proportional to the dynamic stiffness of the structure, the main objective of the controller design is to improve the boring bar dynamic stiffness of all the dominant modes within the limits of the current amplifiers.

A. Control Configurations

The H_∞ optimal control method is chosen for the controller design in this paper because of its advantage in achieving stabilization with optimized frequency response shaping performance. Four different control configurations are proposed to damp the tool tip vibrations, and the system block diagrams are given in Fig. 5. For all the cases, weighting function W_I is used to penalize the closed-loop FRF from cutting force F_c to control current (I) to avoid saturation of the current amplifiers. z_I and z_x are the weighting function outputs, and $K(s)$ is the controller which is synthesized using the H_∞ optimization technique.

Case 1: Armature displacement x is used as a feedback signal for the controller design, and weighing function W_x is used to penalize the closed-loop FRF from cutting force F_c to armature displacement (x) which indirectly reduces the vibration at tool tip (x_t).

Case 2: Armature displacement x is also used for feedback control, but weighing function W_x is used to directly penalize the closed-loop FRF from cutting force F_c to tool tip displacement (x_t).

Case 3: Boring bar acceleration (a) at the accelerometer location (see Fig. 1) is used for feedback control, while weighing function W_x is used to shape the closed-loop FRF from cutting force (F_c) to boring bar displacement (x_a) at the accelerometer location. Similar to Case 1, this method reduces the tool tip vibrations indirectly.

Case 4: The feedback signal is still boring bar acceleration (a), but weighing function W_x is used to directly penalize the closed-loop FRF from cutting force F_c to tool tip displacement (x_t).

The combination of the plant (P_j , $j = 1, 2, 3, 4$) and weighting functions (W_I and W_x) creates a generalized plant which will be used for controller synthesis.

TABLE I
ESTIMATED MODAL PARAMETERS OF THE SYSTEM

Mode #	f_n [Hz]	ζ [%]	$k_{x_t I}$ [A/m]	$k_{x_a I}$ [A/m]	$k_{x I}$ [A/m]	$k_{x_t F}$ [N/m]	$k_{x_a F}$ [N/m]	$k_{x F}$ [N/m]
1	174	1.20	-1.74×10^5	-1.92×10^5	-4.38×10^5	1.62×10^6	1.98×10^6	4.38×10^6
2	614	0.63	1.05×10^6	1.70×10^6	-1.02×10^8	1.72×10^7	2.89×10^7	-4.50×10^8
3	1130	0.18	3.99×10^7	7.23×10^7	-1.90×10^8	2.10×10^7	3.85×10^7	-1.24×10^8

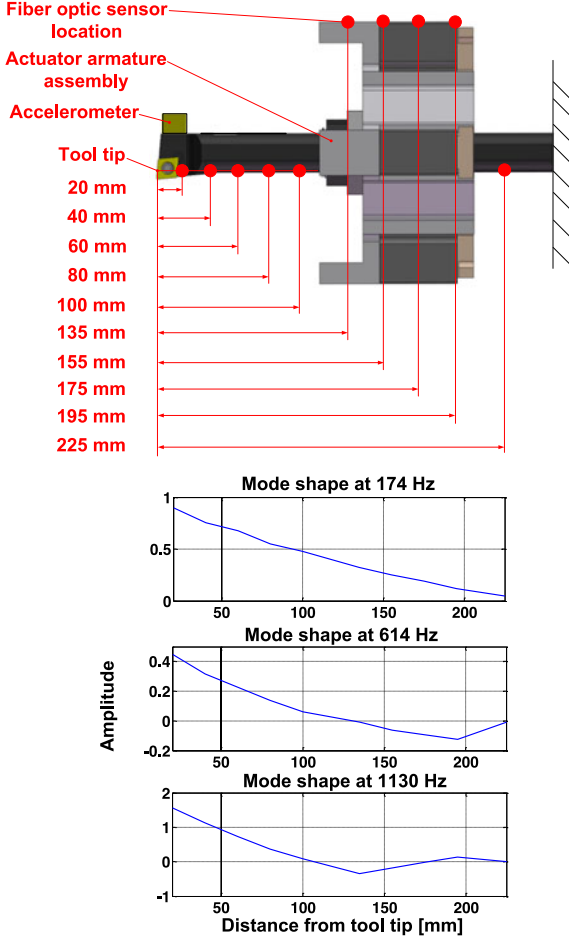


Fig. 4. Mode shape analysis of the boring bar assembly.

B. Guideline for Tuning the Weighting Functions

Both first- and second-order weighting function structures, given in (3), are used for tuning WI and Wx :

$$WI(s), Wx(s) = \begin{cases} K_p \frac{\frac{s}{2\pi f_1} + 1}{\frac{s}{2\pi f_2} + 1} & \text{(first order)} \\ K_p \frac{\left(\frac{s}{2\pi f_1}\right)^2 + \frac{s}{2\pi f_1} + 1}{\left(\frac{s}{2\pi f_2}\right)^2 + \frac{s}{2\pi f_2} + 1} & \text{(second order)} \end{cases} \quad (3)$$

where K_p , f_1 , and f_2 are the tuning parameters of the weighting functions. The weighting functions are tuned so that the peaks in the closed-loop FRF from cutting force F_c to tool tip displacement (x_t) are attenuated as much as possible within the current limits of the amplifiers. Here, a sample guideline for Case 1 is provided for the parameter tuning as an example.

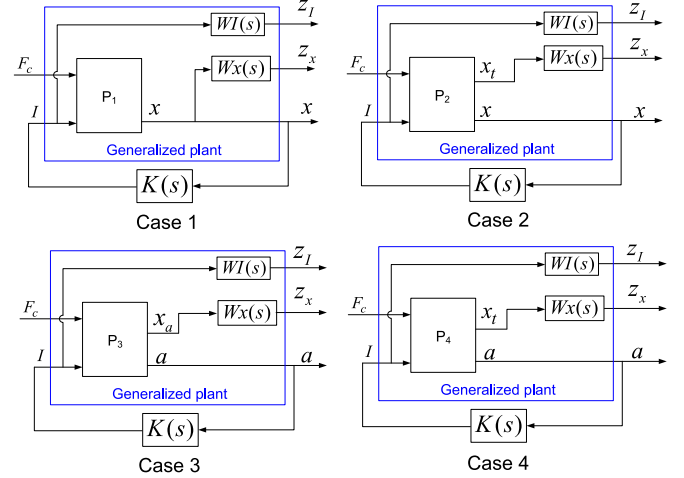


Fig. 5. System block diagrams for controller design.

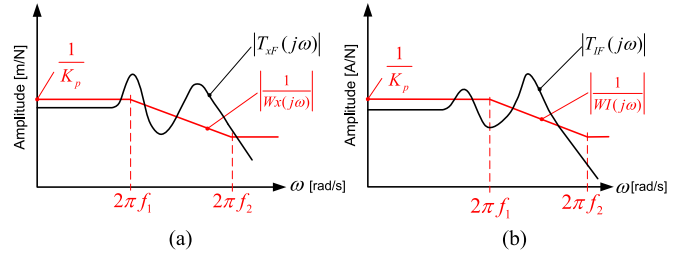


Fig. 6. Schematic diagrams for weighting function selections. (a) $|(Wx)^{-1}|$ and $|T_{xF}|$ in log scale. (b) $|(WI)^{-1}|$ and $|T_{IF}|$ in log scale.

Fig. 6 illustrates how the gain plots of the weighting functions $(Wx)^{-1}$ and $(WI)^{-1}$ affect the FRFs of the closed-loop transfer functions from F_c to x , denoted by T_{xF} , and from F_c to I , denoted by T_{IF} . In order to reduce the peaks of T_{xF} at natural frequency locations, the values of K_p , f_1 and f_2 can be adjusted together to lower the amplitude of $(Wx)^{-1}$ around the peak frequency regions of T_{xF} . Similarly, the amplitude of $(WI)^{-1}$ can be decreased around the peak frequency regions of T_{IF} to penalize the peaks of T_{IF} . If the first-order weighting function cannot give a good control performance, the second-order weighting function can be used in the tuning process. However, a higher amplitude of T_{IF} is normally required to further damp the FRF of T_{xF} . If the amplitude of T_{IF} is too high, it may saturate the current amplifiers during the impact hammer tests and cutting tests, which needs to be avoided during tuning the weighting functions.

TABLE II
WEIGHTING FUNCTION PARAMETERS

Weighting functions	Parameters	Case 1	Case 2	Case 3	Case 4
WI	K_p	10 N/A	14 N/A	30 N/A	40 N/A
	f_1	500 Hz	500 Hz	600 Hz	600 Hz
	f_2	2000 Hz	1600 Hz	2000 Hz	2000 Hz
	order	first order	second order	first order	first order
Wx	K_p	2.4×10^6 N/m	2.0×10^6 N/m	1.0×10^6 N/m	1.0×10^6 N/m
	f_1	165 Hz	200 Hz	200 Hz	160 Hz
	f_2	535 Hz	540 Hz	735 Hz	550 Hz
	order	second order	second order	second order	second order

C. State Space Model of the Generalized Plant

In order to synthesize the controller $K(s)$ using the H_∞ optimization technique, the state space model of the generalized plant is developed as follows.

Since the outputs and the order of the plant are different for the proposed four cases, the state space model of the plant is developed separately for each case, given as:

Case j ($j = 1, 2, 3, 4$):

$$P_j : \begin{cases} [\dot{q}_x] = A_{pj} [q_x] + B_{pj} u \\ y = C_{pj} [q_x] + D_{pj} u \end{cases} \quad (4)$$

$$u = \begin{bmatrix} F_c \\ I \end{bmatrix}, \quad y = \begin{cases} x & (j=1) \\ \begin{bmatrix} x_t \\ x \end{bmatrix} & (j=2) \\ \begin{bmatrix} x_a \\ a \end{bmatrix} & (j=3) \\ \begin{bmatrix} x_t \\ a \end{bmatrix} & (j=4) \end{cases} \quad (5)$$

where q_x is the state vector. Similarly, the state space equations of the weighting functions can also be developed from their transfer functions as follows:

$$WI : \begin{cases} \dot{q}_{WI} = A_{WI} q_{WI} + B_{WI} I \\ z_I = C_{WI} q_{WI} + D_{WI} I \end{cases} \quad (6)$$

$$Wx : \begin{cases} \dot{q}_{Wx} = A_{Wx} q_{Wx} + B_{Wx} u_x \\ z_x = C_{Wx} q_{Wx} + D_{Wx} u_x \end{cases}, \quad (7)$$

$$u_x = \begin{cases} x & (\text{Case 1}) \\ x_t & (\text{Case 2}) \\ x_a & (\text{Case 3}) \\ x_t & (\text{Case 4}) \end{cases} \quad (7)$$

where q_{WI} and q_{Wx} are the state vectors. The derivation processes of the state space models and the system matrices are given in Appendix A.

The state space equation describing the generalized plant for each case can be derived from (4) to (7) as follows:

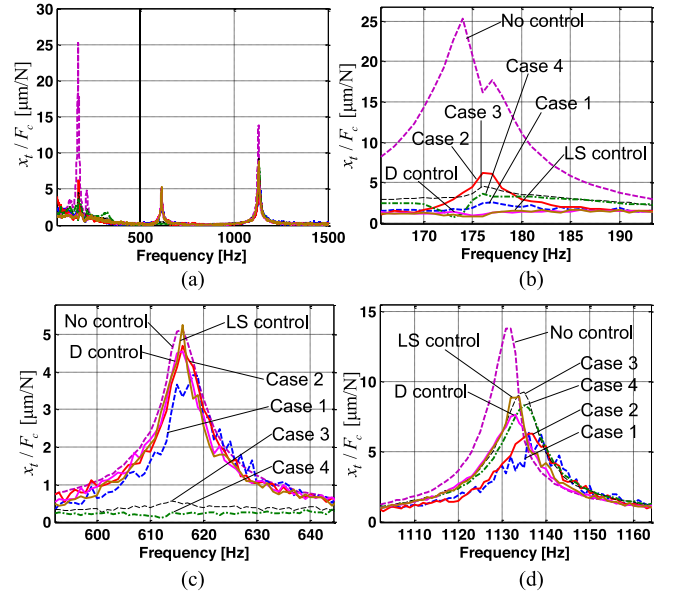


Fig. 7. Measured closed-loop FRFs from cutting force F_c to tool tip displacement (x_t). (a) Full scale FRF. (b) Zoomed-in FRF for mode 1. (c) Zoomed-in FRF for mode 2. (d) Zoomed-in FRF for mode 3.

Case j ($j = 1, 2, 3, 4$):

$$G_{pj} : \begin{cases} \begin{bmatrix} \dot{q}_x \\ \dot{q}_{WI} \\ \dot{q}_{Wx} \end{bmatrix} = \begin{bmatrix} A_{pj} & 0 & 0 \\ 0 & A_{WI} & 0 \\ B_{Wx} C_{nj} & 0 & A_{Wx} \end{bmatrix} \begin{bmatrix} q_x \\ q_{WI} \\ q_{Wx} \end{bmatrix} + \begin{bmatrix} B_{pj} \\ B_W \\ B_{Wx} D_{nj} \end{bmatrix} u \\ \begin{bmatrix} z_I \\ z_x \\ v \end{bmatrix} = \begin{bmatrix} 0 & C_{WI} & 0 \\ D_{Wx} C_{nj} & 0 & C_{Wx} \\ C_{mj} & 0 & 0 \end{bmatrix} \begin{bmatrix} q_x \\ q_{WI} \\ q_{Wx} \end{bmatrix} + \begin{bmatrix} D_W \\ D_{Wx} D_{nj} \\ D_{mj} \end{bmatrix} u \end{cases} \quad (8)$$

$$v = \begin{cases} x & (\text{Cases } j=1, 2) \\ a & (\text{Cases } j=3, 4) \end{cases} \quad (9)$$

TABLE III
TOOL TIP DYNAMIC STIFFNESS FOR DIFFERENT CASES

Cases	Dynamic stiffness at the peaks k_{dn} [N/ μ m]			Minimum dynamic stiffness k_{dn} [N/ μ m]
	first mode (174 Hz)	second mode (614 Hz)	third mode (1130 Hz)	
No control	0.039	0.195	0.073	0.039
D control	0.616	0.220	0.131	0.131
LS control	0.560	0.190	0.112	0.112
Case 1	0.381	0.256	0.159	0.159
Case 2	0.161	0.212	0.158	0.158
Case 3	0.220	1.821	0.108	0.108
Case 4	0.272	3.096	0.120	0.120

TABLE IV
CONTROLLER PARAMETERS

b_i	Case 1	Case 2	Case 3	Case 4	a_i	Case 1	Case 2	Case 3	Case 4
b_0	-2.597×10^{31}	-8.816×10^{54}	2.889×10^{29}	-2.79×10^{50}	a_0	1.103×10^{26}	2.84×10^{49}	4.004×10^{28}	1.869×10^{50}
b_1	2.049×10^{27}	-4.054×10^{51}	4.89×10^{26}	1.147×10^{47}	a_1	8.616×10^{22}	3.807×10^{46}	3.493×10^{27}	4.242×10^{48}
b_2	-9.677×10^{24}	-1.293×10^{49}	4.043×10^{23}	-3.911×10^{44}	a_2	4.399×10^{19}	6.229×10^{43}	1.85×10^{25}	1.519×10^{46}
b_3	9.364×10^{19}	-3.558×10^{45}	-1.375×10^{18}	-4.057×10^{40}	a_3	1.312×10^{16}	5.457×10^{40}	1.179×10^{22}	1.597×10^{43}
b_4	1.137×10^{17}	-4.785×10^{42}	-3.537×10^{15}	-2.105×10^{38}	a_4	2.709×10^{12}	4.098×10^{37}	6.256×10^{18}	2.006×10^{40}
b_5	2.688×10^{14}	-1.068×10^{38}	-7.075×10^{12}	-1.468×10^{35}	a_5	3.343×10^8	2.108×10^{34}	2.056×10^{15}	1.343×10^{37}
b_6	2.109×10^{10}	-1.798×10^{35}	-1.031×10^9	-6.988×10^{31}	a_6	2.196×10^4	8.331×10^{30}	4.749×10^{11}	7.263×10^{33}
b_7	0	6.036×10^{31}	-2.427×10^5	-2.699×10^{28}	a_7	1	2.465×10^{27}	8.619×10^7	2.841×10^{30}
b_8	0	-1.059×10^{28}	-16.31	-6.982×10^{24}	a_8	0	5.903×10^{23}	9717	9.221×10^{26}
b_9	0	8.091×10^{23}	0	-1.792×10^{21}	a_9	0	1.11×10^{20}	1	2.395×10^{23}
b_{10}	0	-2.8×10^{20}	0	-2.704×10^{17}	a_{10}	0	1.75×10^{16}	0	5.113×10^{19}
b_{11}	0	-4.071×10^{15}	0	-4.902×10^{13}	a_{11}	0	2.106×10^{12}	0	9.15×10^{15}
b_{12}	0	-2.072×10^{12}	0	-4.457×10^9	a_{12}	0	2.241×10^8	0	1.249×10^{12}
b_{13}	0	7.717×10^{13}	0	-4.555×10^5	a_{13}	0	1.425×10^4	0	1.579×10^8
b_{14}	0	0	0	-26.27	a_{14}	0	1	0	1.079×10^4
b_{15}	0	0	0	0	a_{15}	0	0	0	1

where $B_W = [0 \ B_{WI}]$, $D_W = [0 \ D_{WI}]$. The matrices C_{nj} , C_{mj} , D_{nj} , and D_{mj} are given in Appendix A.

D. Controller Design

Having the generalized plant, the controller K is synthesized for each case so that the closed-loop system is internally stable and the H_∞ norm of the closed-loop transfer function (T_{zF}) from F_c to z ($z = [z_I \ z_x]^T$) is minimized. This H_∞ optimal control problem can be solved using the linear matrix inequalities (LMI) algorithm presented in [23] with the available MATLAB command hinfscn.m [24]. A brief summary of how to synthesize the H_∞ controller with the LMI method is given in Appendix B.

The weighting function parameters that are used in the controller design are given in Table II.

The transfer function of the synthesized H_∞ optimal controller is obtained as follows:

$$K(s) = \frac{\sum_{i=0}^k b_i s^i}{\sum_{i=0}^k a_i s^i} \quad (10)$$

where k is the order of the controller, and the controller parameters a_i, b_i ($i = 0, 1, 2, \dots, k$) for each case are given in Table IV in Appendix C. The controller order is 7, 14, 9, and 15 for Cases 1, 2, 3, and 4, respectively. It is a summation of the plant order and the order of weighting functions. In equation (1), the order of transfer functions $x_t(s)$, $x_a(s)$, and $x(s)$ are 6, 6, and 4,

respectively. Since only $x(s)$ is needed for Case 1, while $x_a(s)$ is required for Case 3, the plant order in Cases 1 and 3 is much lower, i.e., fourth-order and sixth-order respectively, therefore leading to a lower order controller. On the other hand, because both $x_t(s)$ and $x(s)$ are considered in Case 2, while $x_t(s)$ and $x_a(s)$ are required in Case 4 to model the plant, the plant order in Cases 2 and 4 becomes much higher, i.e., 10th order and 12th order, respectively, therefore leading to a higher order controller.

IV. EXPERIMENTAL RESULTS FOR ACTIVE DAMPING

A. Impact Response Tests

The designed controllers are implemented using the dSPACE 1103 real-time system. A notch filter is added to the controller in Cases 1 and 2 to remove the vibrations around 614 Hz which are not measurable by the fiber optic sensor. The control algorithms used in [20] and [25] are also implemented for comparison, and the controller transfer functions are designed as follows:

$$C_D(s) = (200s) \left(\frac{s^2 + 11.88s + 1.488 \times 10^7}{s^2 + 1131s + 1.488 \times 10^7} \right) \quad (11)$$

$$C_{LS}(s) = 3.47 \times 10^5 \left(1 + \frac{163.67}{s} \right) \left(\frac{1}{15} \frac{\frac{s}{2\pi \times 260.5/15} + 1}{\frac{s}{2\pi \times 260.5/15} + 1} \right) \times \left(\frac{s^2 + 11.88s + 1.488 \times 10^7}{s^2 + 1131s + 1.488 \times 10^7} \right) \quad (12)$$

where C_D and C_{LS} are the derivative (D) controller and loop shaping (LS) controller, respectively.

Impact modal tests were carried out to measure the FRFs from the cutting force F_c to the displacement at the boring bar tip (x_t) for each controller case. The measured FRFs and the tool tip dynamic stiffness at the peaks are shown in Fig. 7 and Table III, respectively. From the measurements, the first bending mode at 174 Hz is completely damped by the controllers. The second mode at 614 Hz is not damped in all the control cases because the fiber optic sensor is at neutral point of this mode. In Cases 3 and 4, however, the second mode is completely damped, since the accelerometer attached close to the tool tip is used, hence the boring bar vibrations contributed by all modes are directly measured. For the third mode at 1130 Hz, the dynamic stiffness is increased considerably for all the control cases. Controller Case 1 achieves better active damping performance over the other control cases. The simple D and LS controllers are normally tuned to be stabilized for the most flexible mode (Mode#1), and cannot provide as good active damping performance as the H_∞ controller as demonstrated in Cases 1 and 2. Due to the noncollocated sensor actuator configuration, the open-loop FRF $G_{x_a I}$ [see Fig. 3(b)], which plays an important role in the plant model in Cases 3 and 4, has a right half-plane zero, which makes the plant a non-minimum phase system, thus limiting the active damping performance. Considering all the three modes, Case 1 gives the highest minimum dynamic stiffness at the tool tip, and therefore provides the best active damping performance. Since not only the damping ratio, but also the modal stiffnesses of the modes are increased with active damping, the natural frequencies of the damped boring bar are higher than the case without active damping.

The closed-loop FRFs from the cutting force F_c to the control current (I) are also measured by giving a hammer blow at the tool tip and measuring the command current to the amplifiers. The measurements are shown in Fig. 8. It can be seen that the third mode at 1130 Hz is much harder to damp compared to the first two modes, since it requires much higher control currents. The results are quite noisy in the control cases in which the armature displacement (x) is used as a feedback signal. This is because the large noise level in the displacement measurements (x) is amplified by the controller and leads to noisy control currents. From Fig. 8, it can be seen that 1 N dynamic cutting force around the third modal frequency of the boring bar demands more than 1 A control current for all the control cases. When the cutting process is stable, the dynamic cutting force will be small due to the low vibration level; therefore, the control current will also be small. However, if chatter happens around the third modal frequency of the controlled boring bar, the large vibrations will lead to very high control currents which can easily saturate the amplifiers. Although it is impossible to damp the third mode completely due to the current limit, its dynamic stiffness is still increased from 0.073 N/ μm to 0.159 N/ μm with controller Case 1.

B. Cutting Tests

The absolute, chatter-free depth of cut (a_{lim}) is proportional to the minimum dynamic stiffness of the boring bar. Since Case 1 has the highest minimum dynamic stiffness, its controller has been used to conduct a series of cutting tests to demonstrate

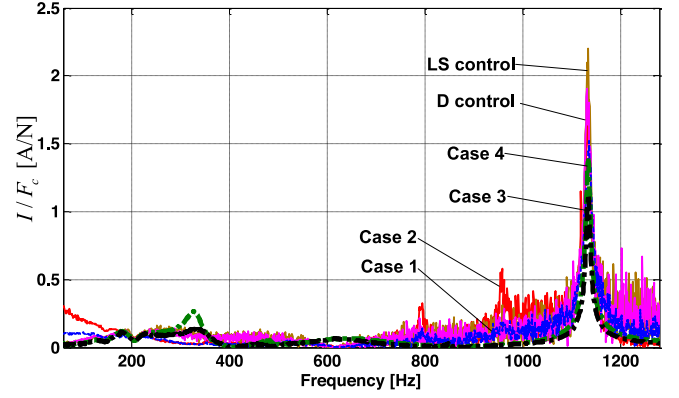


Fig. 8. Measured closed-loop FRFs from cutting force F_c to control current (I).

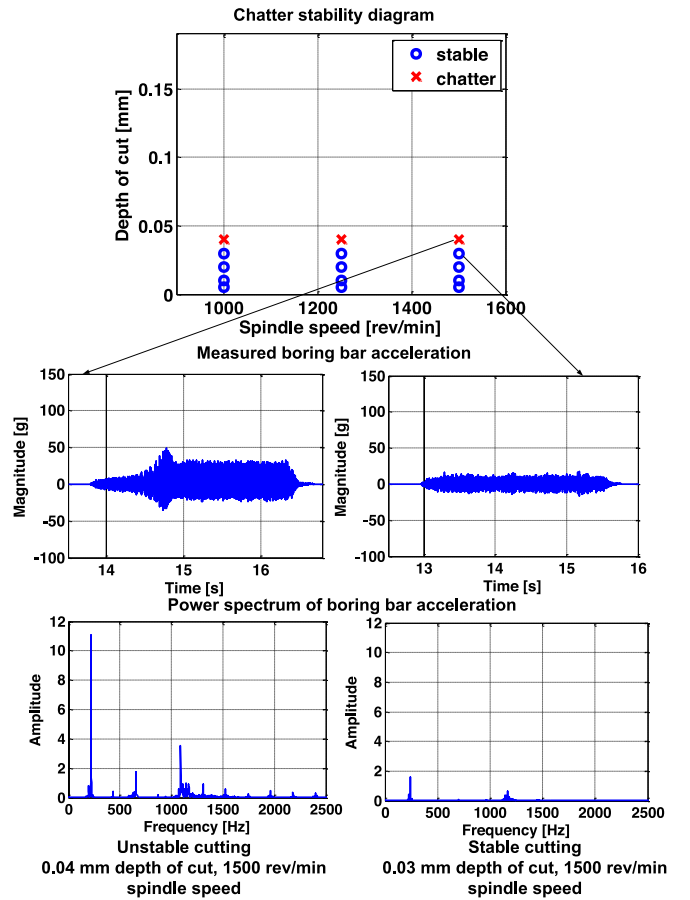


Fig. 9. Chatter stability measurements without active damping.

the viability of active damping to improve chatter-free depth of cuts. The diameter of the hole was increased from 40 to 50 mm with the tool holder described in Section 2.1. The workpiece material is Al6061-T6. The feedrate was 0.2 mm/rev, and the tool has a 0.8 mm nose radius with a 95° approach angle (insert number: CPGT 432). The measured chatter stability charts with and without active damping are compared in Figs. 9 and 10. The presence of chatter is determined from the surface finish and the power spectrum of the measured accelerometer signals.

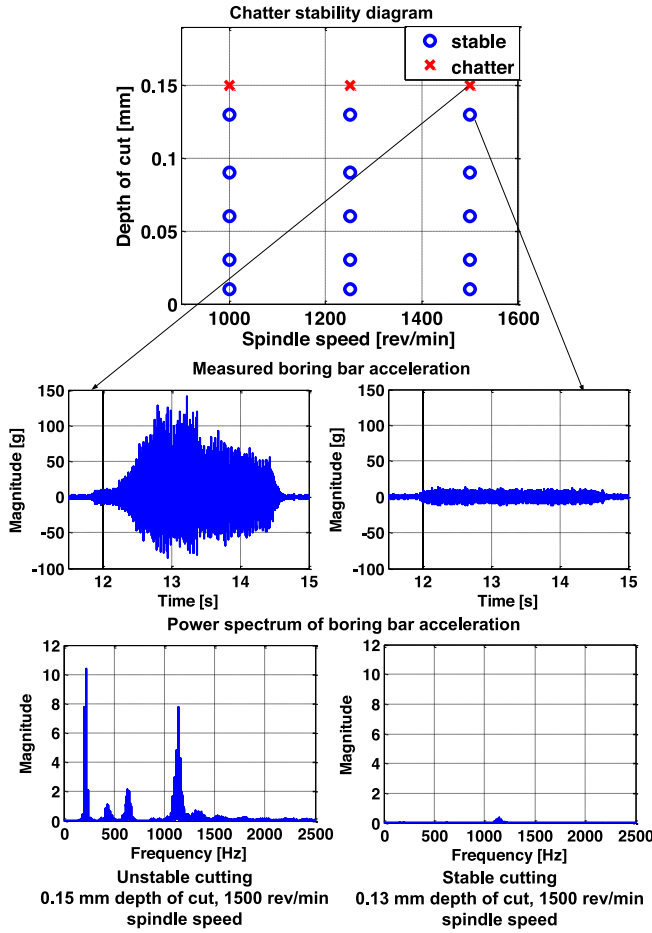


Fig. 10. Chatter stability measurements with active damping.

When there is chatter, the surface finish is rough and the power spectrum has large amplitude peaks at the modal frequencies as shown in Figs. 9 and 10. Without control, the maximum depth of cut is only $a_{lim} = 0.03$ [mm] due to the very high flexibility of the boring bar. The chatter stability is limited by the first bending mode at 174 Hz, which has the lowest dynamic stiffness. The cutting tests were repeated with an actively controlled boring bar. The maximum depth of cut has been increased from 0.03 to 0.13 mm, which is improved by about four times compared to the case without control. Since the first bending mode is damped with active control, the third bending mode of the actively damped boring bar becomes the new limit for chatter stability. At a 0.15 mm depth of cut, the third mode of the controlled boring bar causes chatter and saturates the current amplifiers. The nonlinear saturation significantly limits the control efforts on not only the third mode but also the first mode of the boring bar, which causes both modes to be out of control. Therefore, unstable vibration caused by the first mode of the boring bar starts growing and finally becomes dominant due to higher open-loop flexibility.

Fig. 11 shows the surface finish and the measured surface roughness of the machined workpiece. The workpiece is machined at a 1500 rev/min spindle speed with a 0.04 mm depth of cut. For the case without control, because of chatter, the surface finish of the workpiece is rough with a $35.9 \mu\text{m}$ peak-to-peak

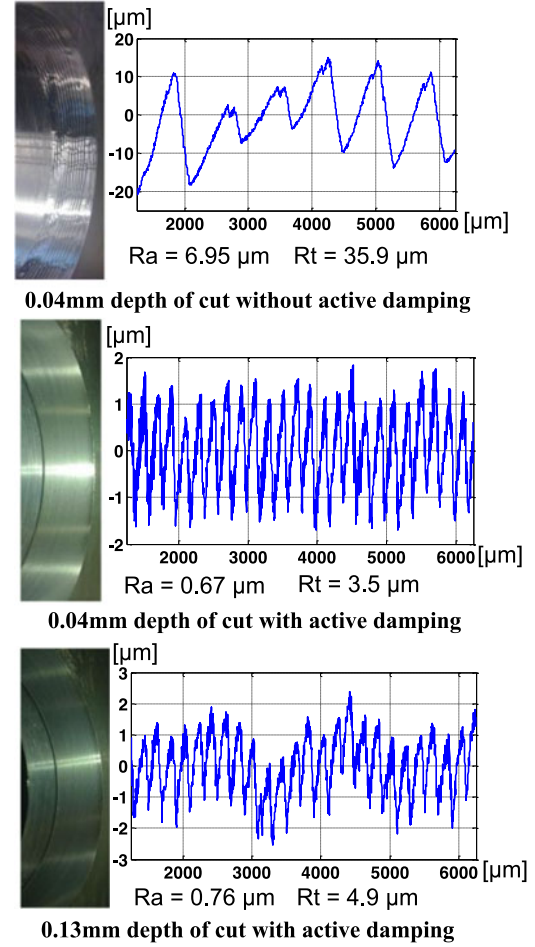


Fig. 11. Surface finish and roughness measurements at spindle speed 1500 rev/min with 0.2 mm/rev feed rate.

height (R_t) and an average roughness (R_a) of $6.95 \mu\text{m}$. When active damping is turned on, the quality of the surface finish is raised significantly ($R_a = 0.67 \mu\text{m}$, $R_t = 3.5 \mu\text{m}$).

Surface finish at a 0.13 mm depth of cut is also measured with active damping. It can be seen that the cutting process is stable and the workpiece has a good surface finish with $R_a = 0.76 \mu\text{m}$ and $R_t = 4.9 \mu\text{m}$. The surface roughness obtained with control at 0.13 mm depth of cut is even better than the stable but uncontrolled cutting at the 0.03 mm small depth of cut ($R_a = 1.56 \mu\text{m}$, $R_t = 9.0 \mu\text{m}$).

V. CONCLUSION

A magnetic actuator is used for the active damping of boring bars. The boring bar vibrations are measured either close to the tool tip via an added accelerometer, or using an existing noncontact, fiber optic displacement sensor within the actuator which is away from the tool tip. An H_∞ optimal control algorithm is applied to the magnetic actuator for all four possible scenarios of vibration suppression methods. It is shown that the use of the actuator's own fiber optic displacement sensor is most effective for damping all modes provided that the sensor location does not coincide with the neutral node of the natural vibration modes. When an accelerometer is attached close to the tool tip as a

feedback sensor, the system becomes a nonminimum phase system due to the noncollocated sensor configuration. The proposed control strategy and magnetic actuator system significantly increases the dynamic stiffness and hence the chatter-free depth of cuts and surface finish, provided that the current amplifier is not saturated in damping high frequency modes.

Although the prototype actuator and control system is proven on simple, cantilevered boring bars in our research laboratory, the concept can be applied to large boring bars, large shafts turned on lathes and machine tool spindles.

APPENDIX A SYSTEM MATRICES OF THE PLANT AND WEIGHTING FUNCTIONS

The state space realization of the plant in (4) is summarized here, taking Case 1 as an example.

Denote:

$$\begin{aligned} x_1(s) &= \frac{G_{p1}}{k_{xI_1}} I(s) + \frac{G_{p1}}{k_{xF_1}} F_c(s) \\ &= \frac{\omega_{n1}^2/k_{xI_1} I(s) + \omega_{n1}^2/k_{xF_1} F_c(s)}{s^2 + 2\zeta_1\omega_{n1}s + \omega_{n1}^2} \end{aligned} \quad (13)$$

$$\begin{aligned} x_3(s) &= \frac{G_{p3}}{k_{xI_3}} I(s) + \frac{G_{p3}}{k_{xF_3}} F_c(s) \\ &= \frac{\omega_{n3}^2/k_{xI_3} I(s) + \omega_{n3}^2/k_{xF_3} F_c(s)}{s^2 + 2\zeta_3\omega_{n3}s + \omega_{n3}^2} \end{aligned} \quad (14)$$

where x_1 and x_3 are the armature displacements caused by the first and third bending modes, respectively. The corresponding differential equations of the system become

$$\begin{aligned} \ddot{x}_1(t) + 2\zeta_1\omega_{n1}\dot{x}_1(t) + \omega_{n1}^2 x_1(t) \\ = \frac{\omega_{n1}^2}{k_{xI_1}} I(t) + \frac{\omega_{n1}^2}{k_{xF_1}} F_c(t) \end{aligned} \quad (15)$$

$$\begin{aligned} \ddot{x}_3(t) + 2\zeta_3\omega_{n3}\dot{x}_3(t) + \omega_{n3}^2 x_3(t) \\ = \frac{\omega_{n3}^2}{k_{xI_3}} I(t) + \frac{\omega_{n3}^2}{k_{xF_3}} F_c(t). \end{aligned} \quad (16)$$

By selecting the state vector $q_x = [\dot{x}_1 \ x_1 \ \dot{x}_3 \ x_3]^T$, the state space model of the plant is obtained for Case 1 as follows:

$$P_1 : \left\{ \begin{aligned} [\dot{q}_x] &= \underbrace{\begin{bmatrix} -2\zeta_1\omega_{n1} & -\omega_{n1}^2 & 0 & 0 \\ 1 & 0 & 0 & 0 \\ 0 & 0 & -2\zeta_3\omega_{n3} & -\omega_{n3}^2 \\ 0 & 0 & 1 & 0 \end{bmatrix}}_{A_{p1}} \\ &\quad \times [q_x] + \underbrace{\begin{bmatrix} \frac{\omega_{n1}^2}{k_{xF_1}} & \frac{\omega_{n1}^2}{k_{xI_1}} \\ 0 & 0 \\ \frac{\omega_{n3}^2}{k_{xF_3}} & \frac{\omega_{n3}^2}{k_{xI_3}} \\ 0 & 0 \end{bmatrix}}_{B_{p1}} \begin{bmatrix} F_c \\ I \end{bmatrix} \\ x &= \underbrace{\begin{bmatrix} 0 & 1 & 0 & 1 \end{bmatrix}}_{C_{p1}} [q_x] + \underbrace{\begin{bmatrix} 0 & 0 \end{bmatrix}}_{D_{p1}} \begin{bmatrix} F_c \\ I \end{bmatrix} \end{aligned} \right. \quad (17)$$

where A_{p1} , B_{p1} , C_{p1} , and D_{p1} are the state space matrices. In the generalized plant model (8), $C_{n1} = C_{m1} = C_{p1}$, $D_{n1} = D_{m1} = D_{p1}$.

The state space matrices of the plant for Cases 2–4 are evaluated similarly.

Case 2:

$$\begin{aligned} A_{p2} &= \begin{bmatrix} A_n & 0 \\ 0 & A_{p1} \end{bmatrix}, B_{p2} = \begin{bmatrix} B_t \\ B_{p1} \end{bmatrix}, \\ C_{p2} &= \begin{bmatrix} C_{n2} \\ C_{m2} \end{bmatrix}, D_{p2} = \begin{bmatrix} D_{n2} \\ D_{m2} \end{bmatrix} \end{aligned} \quad (18)$$

$A_n =$

$$\begin{bmatrix} -2\zeta_1\omega_{n1} & -\omega_{n1}^2 & 0 & 0 & 0 & 0 \\ 1 & 0 & 0 & 0 & 0 & 0 \\ 0 & 0 & -2\zeta_2\omega_{n2} & -\omega_{n2}^2 & 0 & 0 \\ 0 & 0 & 1 & 0 & 0 & 0 \\ 0 & 0 & 0 & 0 & -2\zeta_3\omega_{n3} & -\omega_{n3}^2 \\ 0 & 0 & 0 & 0 & 1 & 0 \end{bmatrix} \quad (19)$$

$$B_t = \begin{bmatrix} \frac{\omega_{n1}^2}{k_{x_t F_1}} & \frac{\omega_{n1}^2}{k_{x_t I_1}} \\ 0 & 0 \\ \frac{\omega_{n2}^2}{k_{x_t F_2}} & \frac{\omega_{n2}^2}{k_{x_t I_2}} \\ 0 & 0 \\ \frac{\omega_{n3}^2}{k_{x_t F_3}} & \frac{\omega_{n3}^2}{k_{x_t I_3}} \\ 0 & 0 \end{bmatrix}, C_{n2} = [C_t \ 0], \quad (20)$$

$$C_t = [0 \ 1 \ 0 \ 1 \ 0 \ 1]$$

$$C_{m2} = [0 \ C_{p1}], \ D_{n2} = D_t,$$

$$D_t = [0 \ 0], \ D_{m2} = D_{p1}. \quad (21)$$

Case 3:

$$A_{p3} = [A_n], B_{p3} = \begin{bmatrix} \frac{\omega_{n1}^2}{k_{x_a F_1}} & \frac{\omega_{n1}^2}{k_{x_a I_1}} \\ 0 & 0 \\ \frac{\omega_{n2}^2}{k_{x_a F_2}} & \frac{\omega_{n2}^2}{k_{x_a I_2}} \\ 0 & 0 \\ \frac{\omega_{n3}^2}{k_{x_a F_3}} & \frac{\omega_{n3}^2}{k_{x_a I_3}} \\ 0 & 0 \end{bmatrix},$$

$$C_{p3} = \begin{bmatrix} C_{n3} \\ C_{m3} \end{bmatrix}, D_{p3} = \begin{bmatrix} D_{n3} \\ D_{m3} \end{bmatrix} \quad (22)$$

$$C_{n3} = [0 \ 1 \ 0 \ 1 \ 0 \ 1] \quad (23)$$

$$\begin{aligned} C_{m3} &= \\ &[-2\zeta_1\omega_{n1} \ -\omega_{n1}^2 \ -2\zeta_2\omega_{n2} \ -\omega_{n2}^2 \ -2\zeta_3\omega_{n3} \ -\omega_{n3}^2] \end{aligned} \quad (24)$$

$$D_{m3} = \left[\frac{\omega_{n1}^2}{k_{x_a F_1}} + \frac{\omega_{n2}^2}{k_{x_a F_2}} + \frac{\omega_{n3}^2}{k_{x_a F_3}} \quad \frac{\omega_{n1}^2}{k_{x_a I_1}} + \frac{\omega_{n2}^2}{k_{x_a I_2}} + \frac{\omega_{n3}^2}{k_{x_a I_3}} \right] \quad (25)$$

$$D_{n3} = \begin{bmatrix} 0 & 0 \end{bmatrix}.$$

Case 4:

$$A_{p4} = \begin{bmatrix} A_n & 0 \\ 0 & A_n \end{bmatrix}, B_{p4} = \begin{bmatrix} B_t \\ B_{p3} \end{bmatrix}, \quad (26)$$

$$C_{p4} = \begin{bmatrix} C_{n4} \\ C_{m4} \end{bmatrix}, D_{p4} = \begin{bmatrix} D_{n4} \\ D_{m4} \end{bmatrix}$$

$$C_{n4} = \begin{bmatrix} C_t & 0 \end{bmatrix}, C_{m4} = \begin{bmatrix} 0 & C_{m3} \end{bmatrix}, \quad (27)$$

$$D_{n4} = D_t, D_{m4} = D_{m3}.$$

The system matrices of the weighting functions are

W_I : (first order)

$$A_{WI} = [-2\pi f_2], B_{WI} = \left[K_p 2\pi f_2 \left(1 - \frac{f_2}{f_1} \right) \right],$$

$$C_{WI} = [1], D_{WI} = \left[K_p \frac{f_2}{f_1} \right]$$

(second order)

$$A_{WI} = \begin{bmatrix} -2\pi f_2 & -(2\pi f_2)^2 \\ 1 & 0 \end{bmatrix}, B_{WI} = \begin{bmatrix} 1 \\ 0 \end{bmatrix},$$

$$D_{WI} = \left[K_p \left(\frac{f_2}{f_1} \right)^2 \right]$$

$$C_{WI} = \left[2\pi K_p \left(\frac{f_2}{f_1} \right)^2 (f_1 - f_2) \quad K_p \left(2\pi \frac{f_2}{f_1} \right)^2 (f_1^2 - f_2^2) \right] \quad (28)$$

W_x : (first order)

$$A_{Wx} = [-2\pi f_2], B_{Wx} = \left[K_p 2\pi f_2 \left(1 - \frac{f_2}{f_1} \right) \right],$$

$$C_{Wx} = [1], D_{Wx} = \left[K_p \frac{f_2}{f_1} \right]$$

(second order)

$$A_{Wx} = \begin{bmatrix} -2\pi f_2 & -(2\pi f_2)^2 \\ 1 & 0 \end{bmatrix}, B_{Wx} = \begin{bmatrix} 1 \\ 0 \end{bmatrix},$$

$$D_{Wx} = \left[K_p \left(\frac{f_2}{f_1} \right)^2 \right]$$

$C_{Wx} =$

$$\left[2\pi K_p \left(\frac{f_2}{f_1} \right)^2 (f_1 - f_2) \quad K_p \left(2\pi \frac{f_2}{f_1} \right)^2 (f_1^2 - f_2^2) \right]. \quad (29)$$

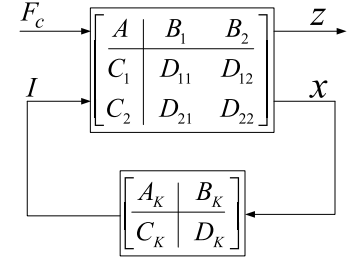


Fig. 12. Reconstructed system block diagram.

APPENDIX B

SUMMARY OF H_∞ CONTROLLER SYNTHESIS WITH THE LMI METHOD

A brief summary of how to synthesize the H_∞ optimal controller using the LMI method [23] is given. Case 1 is used as an example for demonstration. The state space model of the generalized plant (8) can be reconstructed as follows:

$$G_{p1} : \begin{cases} \dot{q} = Aq + \begin{bmatrix} B_1 & B_2 \end{bmatrix} \begin{bmatrix} F_c \\ I \end{bmatrix} \\ \begin{bmatrix} z \\ x \end{bmatrix} = \begin{bmatrix} C_1 \\ C_2 \end{bmatrix} q + \begin{bmatrix} D_{11} & D_{12} \\ D_{21} & D_{22} \end{bmatrix} \begin{bmatrix} F_c \\ I \end{bmatrix} \end{cases} \quad (30)$$

where

$$A = \begin{bmatrix} A_{p1} & 0 & 0 \\ 0 & A_{WI} & 0 \\ B_{Wx} C_{n1} & 0 & A_{Wx} \end{bmatrix},$$

$$B_1 = \begin{bmatrix} \frac{\omega_{n1}^2}{k_{x F_1}} & 0 & \frac{\omega_{n3}^2}{k_{x F_3}} & 0 & 0 & 0 \end{bmatrix}^T,$$

$$B_2 = \begin{bmatrix} \frac{\omega_{n1}^2}{k_{x I_1}} & 0 & \frac{\omega_{n3}^2}{k_{x I_3}} & 0 & B_{WI} & 0 \end{bmatrix}^T,$$

$$C_1 = \begin{bmatrix} 0 & C_{WI} & 0 \\ D_{Wx} C_{n1} & 0 & C_{Wx} \end{bmatrix},$$

$$C_2 = \begin{bmatrix} C_{m1} & 0 & 0 \end{bmatrix},$$

$$D_{11} = \begin{bmatrix} 0 & 0 \end{bmatrix}^T, D_{12} = \begin{bmatrix} D_{WI} & 0 \end{bmatrix}^T,$$

$$D_{21} = 0, \text{ and } D_{22} = 0.$$

Assume the controller K has a transfer function as follows:

$$K(s) = D_K + C_K(sI - A_K)^{-1} B_K \quad (31)$$

where A_K , B_K , C_K , and D_K are the state space matrices of controller K . The system block diagram given in Fig. 5 (Case 1) can be reconstructed with the state space matrices of the generalized plant and the controller, as shown in Fig. 12.

Then, the state space model for the closed-loop transfer function from F_c to z (T_{zF}) can be obtained as follows:

$$\begin{cases} \begin{bmatrix} \dot{q} \\ \dot{q}_k \end{bmatrix} = \underbrace{\begin{bmatrix} A + B_2 D_K C_2 & B_2 C_K \\ B_K C_2 & A_K \end{bmatrix}}_{A_{cl}} \begin{bmatrix} q \\ q_k \end{bmatrix} + \underbrace{\begin{bmatrix} B_1 + B_2 D_K D_{21} \\ B_K D_{21} \end{bmatrix}}_{B_{cl}} F_c \\ z = \underbrace{\begin{bmatrix} C_1 + D_{12} D_K C_2 & D_{12} C_K \end{bmatrix}}_{C_{cl}} \begin{bmatrix} q \\ q_k \end{bmatrix} + \underbrace{[D_{11} + D_{12} D_K D_{21}]}_{D_{cl}} F_c \end{cases} \quad (32)$$

where A_{cl} , B_{cl} , C_{cl} , and D_{cl} are the state space matrices of T_{zF} . Gathering all controller parameters into a single variable gives

$$\Theta = \begin{bmatrix} A_K & B_K \\ C_K & D_K \end{bmatrix}. \quad (33)$$

By introducing the following definitions:

$$\begin{aligned} A_0 &= \begin{bmatrix} A & 0 \\ 0 & 0 \end{bmatrix}; B_0 = \begin{bmatrix} B_1 \\ 0 \end{bmatrix}; C_0 = [C_1 \quad 0]; \\ B_i &= \begin{bmatrix} 0 & B_2 \\ I & 0 \end{bmatrix}; C_i = \begin{bmatrix} 0 & I \\ C_2 & 0 \end{bmatrix}; \\ D_{i1} &= [0 \quad D_{12}]; D_{i2} = \begin{bmatrix} 0 \\ D_{21} \end{bmatrix} \end{aligned} \quad (34)$$

the closed-loop matrices A_{cl} , B_{cl} , C_{cl} , and D_{cl} can be rewritten as [23] follows:

$$\begin{aligned} A_{cl} &= A_0 + B_i \Theta C_i; B_{cl} = B_0 + B_i \Theta D_{i2}; \\ C_{cl} &= C_0 + D_{i1} \Theta C_i; D_{cl} = D_{11} + D_{i1} \Theta D_{i2}. \end{aligned} \quad (35)$$

According to the bounded real lemma for continuous time systems [23], the H_∞ suboptimal constraints can be turned into an LMI problem:

H_∞ suboptimal constraints:

$$\|D_{cl} + C_{cl}(sI - A_{cl})^{-1}B_{cl}\|_\infty < \gamma, (A_{cl} \text{ is stable}) \quad (36)$$

where γ is a predefined positive scalar.

\Leftrightarrow

LMI problem:

There exists a symmetric positive-definite solution X_{cl} to the LMI:

$$\begin{bmatrix} A_{cl}^T X_{cl} + X_{cl} A_{cl} & X_{cl} B_{cl} & C_{cl}^T \\ B_{cl}^T X_{cl} & -\gamma I_1 & D_{cl}^T \\ C_{cl} & D_{cl} & -\gamma I_2 \end{bmatrix} < 0. \quad (37)$$

Then, the controller parameters $\Theta = \begin{bmatrix} A_K & B_K \\ C_K & D_K \end{bmatrix}$ can be

solved by four steps [23].

- 1) Solve the following LMIs for symmetric matrices R and S :

$$\begin{bmatrix} N_R & 0 \\ 0 & I \end{bmatrix}^T \begin{bmatrix} ARA^T - R & ARC_1^T & B_1 \\ C_1 RA^T & -\gamma I + C_1 RC_1^T & D_{11} \\ B_1^T & D_{11}^T & -\gamma I \end{bmatrix} \begin{bmatrix} N_R & 0 \\ 0 & I \end{bmatrix} < 0 \quad (38)$$

$$\begin{bmatrix} N_S & 0 \\ 0 & I \end{bmatrix}^T \begin{bmatrix} A^T SA - S & A^T SB_1 & C_1^T \\ B_1^T SA & -\gamma I + B_1^T SB_1 & D_{11}^T \\ C_1 & D_{11} & -\gamma I \end{bmatrix} \begin{bmatrix} N_S & 0 \\ 0 & I \end{bmatrix} < 0 \quad (39)$$

$$\begin{bmatrix} R & I \\ I & S \end{bmatrix} \geq 0 \quad (40)$$

where N_R and N_S denotes the basis of the null spaces of $[B_2^T, D_{12}^T]$ and $[C_2, D_{21}]$, respectively.

- 2) Find full-column-rank matrices M , N so that:

$$MN^T = I - RS. \quad (41)$$

- 3) Find a unique solution X_{cl} of the linear equation:

$$\begin{bmatrix} S & I \\ N^T & 0 \end{bmatrix} = X_{cl} \begin{bmatrix} I & R \\ 0 & M^T \end{bmatrix}. \quad (42)$$

- 4) Substituting the obtained X_{cl} into (37) and solve the inequality for the controller parameters $\Theta = \begin{bmatrix} A_K & B_K \\ C_K & D_K \end{bmatrix}$.

By using a standard γ -iteration technique, the optimal value of γ and the corresponding controller parameters Θ of the H_∞ optimal controller can be obtained.

APPENDIX C

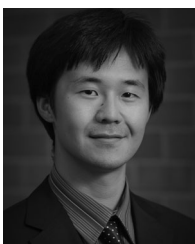
PARAMETERS OF THE DESIGNED H_∞ CONTROLLERS

The controller parameters a_i , b_i ($i = 0, 1, 2, \dots, k$) for each case are given in Table IV.

REFERENCES

- [1] L. K. Rivin and H. L. Kang, "Improving dynamic performance of cantilever boring bars," *Ann. CIRP*, vol. 38, no. 3, pp. 377–380, Jan. 1989.
- [2] B. Godfrey, "Power-generation components make new demands on tooling," *Energy Manuf.*, pp. 71–73, 2011.
- [3] M. H. Miguélez, L. Rubio, J. A. Loya, and J. Fernández-Sáez, "Improvement of chatter stability in boring operations with passive vibration absorbers," *Int. J. Mech. Sci.*, vol. 52, no. 10, pp. 1376–1384, Jul. 2010.
- [4] Y. Yang, J. Munoa, and Y. Altintas, "Optimization of multiple tuned mass dampers to suppress machine tool chatter," *Int. J. Mach. Tools Manuf.*, vol. 50, no. 9, pp. 834–842, May 2010.

- [5] H. Tanaka, F. Obata, T. Matsubara, and H. Mizumoto, "Active chatter suppression of slender boring bar using piezoelectric actuators," *JSME Int. J.*, vol. 37, no. 3, pp. 601–806, 1994.
- [6] J. Redmond, P. Barney, and D. Smith, "Development of an active boring bar for increased chatter immunity," *Proc. SPIE*, vol. 3044, pp. 295–306, 1997.
- [7] J. R. Pratt and A. H. Nayfeh, "Chatter control and stability analysis of a cantilever boring bar under regenerative cutting conditions," *Philosoph. Trans. Roy. Soc. Lond. A*, vol. 359, pp. 759–792, 2001.
- [8] E. Abele, Y. Altintas, and Y. Brecher, "Machine tool spindle units," *Ann. CIRP*, vol. 59, no. 2, pp. 781–802, 2010.
- [9] Y. Cao, L. Cheng, X. B. Chen, and J. Y. Peng, "An inversion-based model predictive control with an integral-of-error state variable for piezoelectric actuators," *IEEE/ASME Trans. Mechatronics*, vol. 18, no. 3, pp. 895–904, Jun. 2013.
- [10] G. Gu, L. Zhu, C. Su, and H. Ding, "Motion control of piezoelectric positioning stages: Modeling, controller design, and experimental evaluation," *IEEE/ASME Trans. Mechatronics*, vol. 18, no. 5, pp. 1459–1471, Oct. 2013.
- [11] M. N. Islam and R. J. Seethaler, "Sensorless position control for piezoelectric actuators using a hybrid position observer," *IEEE/ASME Trans. Mechatronics*, vol. 19, no. 2, pp. 667–675, Apr. 2014.
- [12] M. Al Janaideh and P. Krejci, "Inverse rate-dependent prandtl-ishlinskii model for feedforward compensation of hysteresis in a piezomicro-positioning actuator," *IEEE/ASME Trans. Mechatronics*, vol. 18, no. 5, pp. 1498–1507, Oct. 2013.
- [13] R. J. E. Merry, J. L. Holierhoek, M. J. G. Van De Molengraft, M. Steinbuch, and S. Member, "Gain scheduling control of a walking piezo actuator," *IEEE/ASME Trans. Mechatronics*, vol. 19, no. 3, pp. 954–962, Jun. 2014.
- [14] C. Micromixing, "Iterative control of piezoactuator for evaluating biomimetic, cilia-based micromixing," *IEEE/ASME Trans. Mechatronics*, vol. 18, no. 3, pp. 944–953, Jun. 2013.
- [15] D. M. Neal and H. H. Asada, "Bipolar piezoelectric buckling actuators," *IEEE/ASME Trans. Mechatronics*, vol. 19, no. 1, pp. 9–19, Feb. 2014.
- [16] J. Y. Peng and X. B. Chen, "Integrated PID-based sliding mode state estimation and control for piezoelectric actuators," *IEEE/ASME Trans. Mechatronics*, vol. 19, no. 1, pp. 88–99, Jan. 2014.
- [17] Y. Qin, Y. Tian, D. Zhang, and B. Shirinzadeh, "A novel direct inverse modeling approach for hysteresis compensation of piezoelectric actuator in feedforward applications," *IEEE/ASME Trans. Mechatronics*, vol. 18, no. 3, pp. 981–989, Jun. 2013.
- [18] M. Chen and C. R. Knospe, "Control approaches to the suppression of machining chatter using active magnetic bearings," *IEEE Trans. Control Syst. Technol.*, vol. 15, no. 2, pp. 220–232, Mar. 2007.
- [19] N. J. M. Van Dijk, N. Van De Wouw, E. J. J. Doppenberg, J. A. J. Oosterling, and H. Nijmeijer, "Robust active chatter control in the high-speed milling process," *IEEE Trans. Control Syst. Technol.*, vol. 20, no. 4, pp. 901–917, Jul. 2012.
- [20] X. D. Lu, F. Chen, and Y. Altintas, "Magnetic actuator for active damping of boring bars," *CIRP Ann.*, vol. 63, no. 1, pp. 369–372, 2014.
- [21] X. D. Lu and D. L. Trumper, "Ultrafast tool servos for diamond turning," *Ann. CIRP*, vol. 54, no. 1, pp. 383–388, 2005.
- [22] I. Lazoglu, F. Atabey, and Y. Altintas, "Dynamics of boring processes: Part III-time domain modeling," *Int. J. Mach. Tools Manuf.*, vol. 42, no. 14, pp. 1567–1576, 2002.
- [23] P. Gahinet and P. Apkarian, "A linear matrix inequality approach to H_∞ control," *Int. J. Robust Nonlinear Control*, vol. 4, no. 4, pp. 421–448, 1994.
- [24] *Documentation*, The MathWorks, Inc., Natick, MA, USA, 2012 [Online]. Available: <http://www.mathworks.com>
- [25] F. Chen, X. D. Lu, and Y. Altintas, "A novel magnetic actuator design for active damping of machining tools," *Int. J. Mach. Tools Manuf.*, vol. 85, pp. 58–69, 2014.



Fan Chen received the B.A.Sc. degree in mechanical engineering from Tsinghua University, Beijing, China, in 2008, and the M.A.Sc. degree from the National University of Defense Technology, Changsha, Hunan, China. He is currently working toward the Ph.D. degree in mechanical engineering at The University of British Columbia, Vancouver, BC, Canada.

His research interests include magnetic actuator design, control, and active damping of machine tool vibration.



Masih Hanifzadegan (S'13) received the B.S. and M.S. degrees from the Department of Mechanical Engineering, Amirkabir University of Technology (Tehran Polytechnic), Tehran, Iran, in 2006 and 2009, respectively. He is currently working toward the Ph.D. degree in mechanical engineering at The University of British Columbia, Vancouver, BC, Canada.

From April to August 2013, he was an Intern at the Fraunhofer Institute for Machine Tools and Forming Technology, Chemnitz, Germany. His research interests include robust control theory and its applications to serial and parallel machine tools, structural vibration, and active noise control.

Mr. Hanifzadegan received the Wendy Fan Memorial Scholarship in 2011, and the Strategic Network Enhancement Initiative Award from the Natural Sciences and Engineering Research Council of Canada.

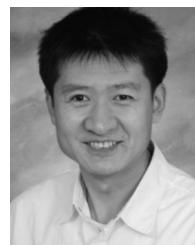


Yusuf Altintas received the Ph.D. degree in mechanical engineering from McMaster University, Hamilton, ON, Canada, in 1987.

He joined The University of British Columbia, Vancouver, BC, Canada, and founded the Manufacturing Automation Laboratory in 1986. He is currently a Professor in the Mechanical Engineering Department at The University of British Columbia. He conducts research on metal cutting mechanics, machine tool vibrations, digital control of machine tools and virtual machining. He has published more than

140 archival journal articles and the widely used *Manufacturing Automation: Principles of Metal Cutting Mechanics, Machine Tool Vibrations and CNC Design* (Cambridge, U.K.: Cambridge University Press, 2000, 2012).

Dr. Altintas is a Fellow of the Royal Society of Canada, Canadian Academy of Engineering, American Society of Mechanical Engineers, SME, and CIRP. He received honorary doctorate degrees from the Stuttgart and Budapest Technical Universities, the Gold Medal of Engineers Canada and the top scientific prize of Turkey. He currently directs the NSERC CANRIMT Machining Research Network across Canada. He holds the NSERC—P&WC Industrial Research Chair Professorship to develop next-generation virtual high-performance machining technology.



Xiaodong Lu (M'05) received the B.S. and M.S. degrees in automotive engineering from Tsinghua University, Beijing, China, in 1997 and 1999, respectively, and the Ph.D. degree in mechanical engineering from the Massachusetts Institute of Technology (MIT), Cambridge, MA, USA, in 2005.

In 2005, he joined the Department of Mechanical Engineering, University of British Columbia, Vancouver, BC, Canada, where he is currently an Associate Professor. His teaching and research interests include control, electromechanics, electronics, manufacturing equipment and instrument, mechatronics, precision machine design, precision metrology, and real-time computing systems.

Dr. Lu is a member of the ASME and ASPE. His awards include the Top Grade Award from Tsinghua University in 1996 for being among the university's top three undergraduate students, the Carl G. Sontheimer Prize from MIT in 2005 for excellence in innovation and creativity in design, and the F.W. Taylor Medal from CIRP (International Academy for Production Engineering) in 2007 for outstanding merit in original scientific research work on ultrafast tool servos.